Human Molecular Genetics, 2016, Vol. 25, No. 23 5111–5125

doi: 10.1093/hmg/ddw315
Advance Access Publication Date: 16 September 2016
Original Article

ORIGINAL ARTICLE

Reep1 null mice reveal a converging role for hereditary spastic paraplegia proteins in lipid droplet regulation

Benoît Renvoisé[1], Brianna Malone[1], Melanie Falgairolle[2],
Jeeva Munasinghe[3], Julia Stadler[1], Caroline Sibilla[1,†], Seong H. Park [1] and
Craig Blackstone[1,*]

[1]Cell Biology Section, Neurogenetics Branch, [2]Developmental Neurobiology Section and [3]Laboratory of Functional and Molecular Imaging, National Institute of Neurological Disorders and Stroke, National Institutes of Health, Bethesda, Maryland, USA

[*]To whom correspondence should be addressed at: Craig Blackstone, Neurogenetics Branch, NINDS, NIH, Building 35, Room 2A-201, 9000 Rockville Pike, Bethesda, MD 20892-3738, USA. Tel: +1 3014519680; Fax: +1 3014804888; E-mail: blackstc@ninds.nih.gov

Abstract

Hereditary spastic paraplegias (HSPs; SPG1-76 plus others) are length-dependent disorders affecting long corticospinal axons, and the most common autosomal dominant forms are caused by mutations in genes that encode the spastin (SPG4), atlastin-1 (SPG3A) and REEP1 (SPG31) proteins. These proteins bind one another and shape the tubular endoplasmic reticulum (ER) network throughout cells. They also are involved in lipid droplet formation, enlargement, or both in cells, though mechanisms remain unclear. Here we have identified evidence of partial lipoatrophy in *Reep1* null mice in addition to prominent spastic paraparesis. Furthermore, *Reep1-/-* embryonic fibroblasts and neurons in the cerebral cortex both show lipid droplet abnormalities. The apparent partial lipodystrophy in *Reep1* null mice, although less severe, is reminiscent of the lipoatrophy phenotype observed in the most common form of autosomal recessive lipodystrophy, Berardinelli-Seip congenital lipodystrophy. Berardinelli-Seip lipodystrophy is caused by autosomal recessive mutations in the *BSCL2* gene that encodes an ER protein, seipin, that is also mutated in the autosomal dominant HSP SPG17 (Silver syndrome). Furthermore, REEP1 co-immunoprecipitates with seipin in cells. This strengthens the link between alterations in ER morphogenesis and lipid abnormalities, with important pathogenic implications for the most common forms of HSP.

Introduction

Hereditary spastic paraplegias (HSPs) are characterized by prominent lower extremity spasticity and typically more mild weakness, resulting from a length-dependent axonopathy of corticospinal motor neurons (1–5). Historically, HSPs have been classified as ‘pure’ or ‘complicated’ based on the absence (pure) or presence (complicated or complex) of additional clinical features including distal amyotrophy, ataxia, neuropathy, parkinsonism, cognitive changes, or visual changes, among others. More recently a genetic classification scheme has predominated, and HSPs are most often referred to by their genetic loci (numbered in order of identification, SPG1-76). Still others have not been assigned an SPG locus (1–4,6). To date, over 60 HSP gene products have been identified, and functional analyses support pathogenic convergence within a relatively small number of common cellular themes (2).

SPG4, SPG3A and SPG31 are the most common autosomal dominant HSPs (listed in order of frequency), together comprising ~50% of all patients with HSP. Indeed, the three disease

---

[†]Present address: MRC Laboratory of Molecular Biology, Cambridge, UK.

Received: May 25, 2016. **Revised:** August 4, 2016. **Accepted:** September 12, 2016

gene products atlastin-1, spastin and receptor expression-enhancing protein 1 (REEP1), respectively, together with the SPG72 protein REEP2, SPG12 protein reticulon 2, SPG61 protein ARL6IP1 and SPG69 protein RAB3GAP2, play roles in shaping and distributing the tubular endoplasmic reticulum (ER) network in cells (2,6–8). REEP1, atlastin-1 and the larger, membrane-bound M1 isoform of spastin interact through hydrophobic hairpin domains within the tubular ER to coordinate ER shaping and microtubule interactions (7,9–12). Interestingly, atlastin-1, spastin and REEP1 localize prominently to the corticospinal neurons whose axons are impaired in HSPs (13–17).

SPG31 results from autosomal dominant *REEP1* mutations (18). It is mostly a pure form only rarely associated with neuropathy, and in just one family was an axonal neuropathy present without signs of hyperreflexia. Some mutations disrupt a predicted miRNA binding site in the 3’ untranslated region, supporting haploinsufficiency in at least a subset of patients, and heterozygous missense and truncation mutations have also been described throughout the gene (18,19). A young boy with a homozygous loss-of-function mutation presented with a spinal muscular atrophy with respiratory distress type 1 (SMARD1)-like phenotype, with additional features of congenital axonal neuropathy, hyperreflexia and diaphragmatic palsy (20).

REEP proteins were first described based on their ability to enhance surface expression of some G-protein coupled receptors, including olfactory and taste receptors (21,22). REEP1 is a member of a family of ER shaping proteins comprising six members in humans, divided structurally and functionally into two main subgroups, REEP1-4 and REEP5-6 (7,23,24), with REEP1-4 proteins involved in microtubule interactions with ER tubules (7,25). REEP1 has also been reported to facilitate ER-mitochondrial interactions (26). Finally, REEP proteins have also been implicated in enhancing ER cargo capacity, regulating ER-Golgi processing and interacting selectively with some cargo proteins (23). Given these numerous functional roles, the *in vivo* consequences of REEP1 mutation remain largely unknown.

The ER is a continuous membrane organelle comprising the nuclear envelope and a peripheral network of membrane tubules and sheets (27,28). Tubular ER presents high membrane curvature in cross-section stabilized by members of the reticulon and REEP protein families (10,11), likely by forming wedge-like structures in the lipid bilayer as well as arc-like scaffolds around tubules (10,11,24,28). Identifying effects of changes in ER morphology thus appears critical for understanding HSP pathologic mechanisms. Of course, this is complicated by the fact that the ER has many different functions and interactions with numerous organelles and cytoskeletal elements (27,28).

Recent attention has focused on the role of the ER in the formation of lipid droplets (LDs), organelles involved in fat storage in eukaryotes (29). LDs contain a core of neutral lipids (triglycerides and sterol esters) surrounded by a phospholipid monolayer containing proteins such as perilipins. Interestingly, atlastin-1 regulates LD size, with REEP1 also playing a role, albeit less clear (30,31). Furthermore, the HSP proteins seipin (SPG17), spartin (SPG20) and spastin (SPG4) also function in LD maintenance, indicating a possible convergent pathogenic theme (2,32). Atlastin-1 and REEP1 can be co-immunoprecipitated from cells (7), and SPG17 protein seipin (Fld1p in yeast) is a conserved integral membrane ER protein thought to act at the interface of the ER and LDs (33). Recently, overexpressed atlastin-1 has been co-precipitated with the SPG73 gene product CPT1C, an ER-localized carnitine palmitoyltransferase (34).

Here we report that *Reep1-/-* mice exhibit a gait phenotype and prominent spasticity, along with significant lipodystrophy. These symptoms are associated with prominent changes in cellular LDs. Reep1 localizes to the ER and interacts with atlastin-1 as well as with the SPG17 protein seipin that is also mutated in the most common form of autosomal recessive lipodystrophy, Berardinelli-Seip congenital lipodystrophy, suggesting a model whereby REEP1 may function with other key HSP gene products to regulate LD formation and size.

Results

Reep1-/- mice exhibit spasticity and motor dysfunction

Reep1-/- mice were generated as shown in Supplementary Material, Figure S1A, and disruption of the *Reep1* gene was confirmed using PCR (Supplementary Material, Fig. S1B). Immunoblotting of multiple mouse tissues established the absence of the Reep1 protein (Supplementary Material, Fig. S1C). *Reep1-/-* mice bred normally, and their offspring appeared normal at birth. Early in life they moved throughout the cage much like littermate controls and appeared to feed normally. However, they soon developed age-dependent impairments in motor function. Compared to wild-type animals, *Reep1-/-* mice exhibited spasticity, with lower extremity clonus at postnatal day 3 (compare Supplementary Material, Videos S1 and S2), prominent impairment at 2 months in the Rotarod test (Fig. 1A), and significant differences in gait parameters such as stride time, stance time and stance length upon formal TreadScan testing (Fig. 1A and Supplementary Materials, Fig. S1D and Movies S3–S7). However, grip test data showed no differences (Supplementary Material, Fig. S1E). At 4 months, ∼50% of *Reep1-/-* mice were unable to walk at the same speed as *Reep1+/+* mice. Thus, *Reep1-/-* mice have a progressive defect in ambulation reminiscent of that in SPG31 patients, as reported previously (17). In preliminary studies, *Reep1+/-* animals had essentially no phenotype even at more advanced ages (data not shown), also consistent with a previous report (17), and they were not investigated further.

Reep1-/- motoneurons exhibit increased activity

Gait dysfunction affecting the hind limbs in mice can result from different types of impairments in the pyramidal motor pathway. To understand the basis for the *Reep1-/-* phenotype neurophysiologically, we analysed motoneuron activity (35). In 3-day-old *Reep1-/-* mice, locomotor-like activity frequency was higher (Fig. 1B, Supplementary Material, Fig. S1F–H). Also, latency of the suprathreshold monosynaptic reflex (L5 segment) was shortened in *Reep1-/-* mice (Fig. 1C–E, Supplementary Material, Fig. S1F and H), independent of the site of stimulation (Supplementary Material, Fig. S1H). Together, these data support spasticity as a principal cause of the impaired gait in the *Reep1-/-* mice. Motoneuron staining using fluorescent dyes also showed that the *Reep1-/-* lateral motor pool is slightly smaller (Fig. 1F and G). Intracellular input resistances recorded from *Reep1-/-* and *Reep1+/+* motoneurons were not different, however, suggesting that *Reep1-/-* motoneuron input resistance changes are either due to a decrease in the extent of the dendritic tree or else increased membrane resistivity. Monosynaptic reflexes did not show differences intracellularly (Supplementary Material, Fig. S1F and H).

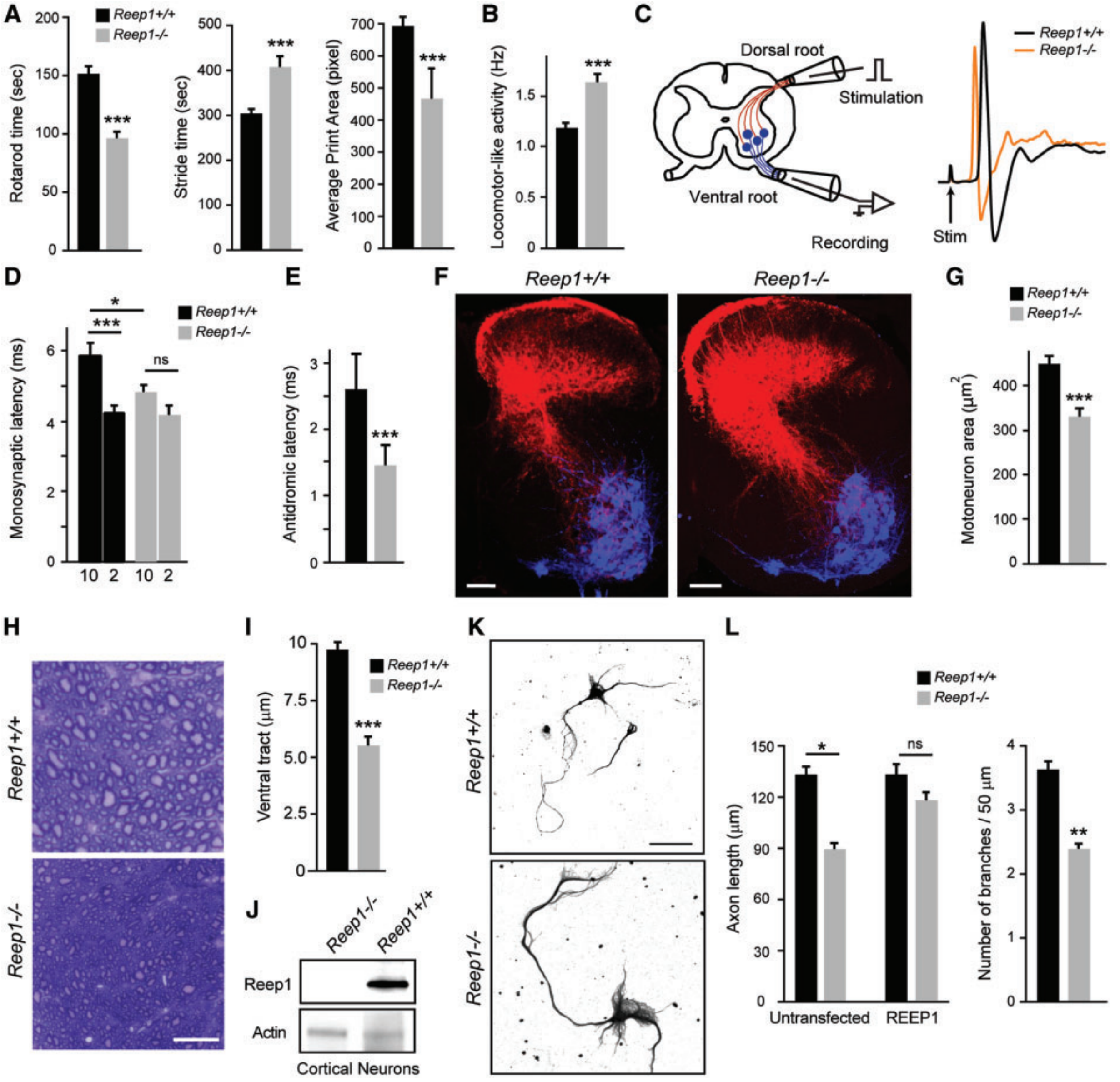

Figure 1. *Reep1*-/- mice exhibit motor dysfunction and axon abnormalities. (**A**) Rotarod duration testing of *Reep1*+/+ and *Reep1*−/− mice at 2 months ($n = 20$). Stride time and print area were obtained using a TreadScan Gait device (speed = 14 cm/sec; $n = 20$); means ± SEM. $^{***}P < 0.001$. (**B**) Frequencies of locomotor-like activity evoked by 10× threshold train of stimuli to dorsal root ganglion. $^{***}P < 0.001$. (**C**) Measurement of monosynaptic reflex latency from L5 ventral root. Left, Experimental set-up; motoneurons are blue and afferents are red. Right, Superimposed traces showing averaged monosynaptic reflexes recorded in one *Reep1*+/+ and one *Reep1*-/- animal. (**D**) Average monosynaptic latencies for 2× and 10× thresholds. Means ± SEM; $^{*}P < 0.05$, $^{***}P < 0.001$. ns, not significant. (**E**) Antidromic latencies of intracellularly-recorded L5 motoneurons. (**F**) Transverse L5 spinal cord sections showing dorsal root fibres filled with fluorescent dextran (red), with motoneurons in blue. Scale bar, 100 μm. (**G**) Mean sizes ± SEM of L5 motoneurons calculated from **F**. $^{***}P < 0.001$. (**H**) Microslice 100 μm sections of cervical spinal cord from 4-month old mice were stained with toluidine blue. Scale bar, 100 μm. (**I**) Axon diameters in the ventral tract (means ± SEM; $n = 3$). $^{***}P < 0.001$. (**J**) Immunoblot of Reep1 protein in lysates from cortical neurons, with actin as a loading control. (**K**) Representative DIV6 cortical neurons were stained for β-tubulin (black). Scale bar, 20 μm. (**L**) Left, Quantifications of primary axon length in DIV3 neurons (means ± SEM; $n = 3$, with 30 neurons per trial), with overexpression of REEP1 where indicated. $^{*}P < 0.05$. ns, not significant. Right, Quantifications of primary axon branches in neurons (means ± SEM; $n = 3$, with 30 neurons per trial). $^{**}P < 0.01$.

Disruption of the *Reep1* gene causes reduction in neuronal axon length and decreased branching

Four month-old male *Reep1*−/−, *Reep1*+/+ and *Reep1*+/- mice were phenotyped pathologically (NIH Veterinary Research Program), with no gross differences in particular within the CNS. Similarly, more detailed evaluations of sections through cerebral cortex and spinal cord revealed no obvious differences in *Reep1*-/- mice (Supplementary Material, Fig. S2). To assess the Reep1 developmental expression in the CNS, we measured mRNA levels of Reep1 and its closest orthologue Reep2 in several regions, at multiple time points (Supplementary Material, Fig. S3). Reep1 mRNA expression is particularly high in the cerebral cortex at post-natal day 7 (P7), while Reep2 expression is more constant throughout the CNS and during development.

The overall structure of the spinal cord and numbers of anterior horn cells are not changed in *Reep1*-/- mice (Supplementary Material, Fig. S2C and E). However, myelin staining of thoracic spinal cord sections from 4-month-old *Reep1-/-* mice revealed visible degeneration, and quantifications showed a significant reduction in axon diameter in both ventral and dorsal tracts of *Reep1-/-* spinal cord (Fig. 1H and I and Supplementary Material, Fig. S1G). A number of mammalian cell culture models for HSPs have exhibited alterations in axon elongation and branching; therefore, we analysed effects of Reep1 loss on axon outgrowth in cultured cortical neurons at 6 days *in vitro* (DIV) (Fig. 1J–L). Axon length and branch numbers were significantly reduced in *Reep1-/-* neurons, an effect rescued upon expression of recombinant human REEP1 (Fig. 1L).

Reep1 disruption leads to lipoatrophy

While there were no differences in body weight (Supplementary Material, Fig. S4A), visually *Reep1-/-* mice appeared thinner (Fig. 2A) and torso dissection showed a significant reduction of the fat tissue (Fig. 2B). Though gross structures of white adipose (WAT) and liver tissues seemed similar (Fig. 2C, Supplementary Material, Fig. S4B), the proportion of total adipose tissue measured by body CT scan was significantly decreased in *Reep1−/−* male mice (Fig. 2D and E). To establish whether there were direct effects of Reep1 loss in fat tissue, we performed immunoblotting. Reep1 was absent in *Reep1−/−* fat, but present in *Reep1+/+*, and Reep2 levels were also markedly decreased in *Reep1−/−* fat (Fig. 2F). This is likely not due to widespread changes in ER shaping proteins, since *Reep1-/-* mice had no differences in levels of the ER protein Reep5 (Supplementary Material, Fig. S4C). Finally, fasting triglyceride, cholesterol and insulin levels were also significantly reduced in *Reep1-/-* serum (Fig. 3A, Supplementary Material, Fig. S2A), consistent with dyslipidemia but not the commonly observed pattern of hypercholesterolemia and hypertriglyceridemia typically associated with human lipodystrophies.

We next examined whether expression of Reep1 was associated with adipogenesis regulation in WAT from *Reep1-/-* and *Reep1+/+* mice using qPCR. The expression of many pro-adipogenesis markers, such as Cebpd, Dkk1, Fgf2 and Jun, was significantly reduced (Fig. 3B). In contrast, expressions of anti-adipogenic such as Foxo1 and Taz1 were significantly upregulated in *Reep1-/-* mice compared to *Reep1+/+* mice (Fig. 3C), consistent with our earlier observation that *Reep1-/-* mice exhibit a significant reduction of adipose tissue accumulation. Together, these findings suggest that Reep1 acts during adipocyte differentiation to regulate adipogenesis, possibly via its binding partners in the ER.

Lipid changes in *Reep1-/-* brain

To assess any roles of Reep1 in CNS lipid metabolism, we examined lipid profiles in brain of *Reep1−/−* and *Reep1+/+* animals *in vivo*. Importantly, SPG54 patient brains have an abnormal lipid peak on MR spectroscopy (36). While *Reep1+/+* and *Reep1-/-* mice had a similar overall lipid spectrum, our analysis of MRI T_2 values from several brain regions revealed significant alterations in *Reep1-/-* cerebral cortex, suggesting that water/lipid compositions are altered. This reduction appeared selective, since MRI T_2 values in other regions were not different (Fig. 4A, Supplementary Material, Fig. S4D–E). In addition, in the *Reep1-/-* mice numerous metabolite levels were higher, in particular glutamate (Supplementary Material, Fig. S4E–G). Together, these results support a role for Reep1 in CNS lipid metabolism, particularly in cerebral cortex.

Reep1-/- cells have LD defects and altered ER morphology

Several groups have shown that overexpressed REEP1 is involved in shaping ER tubules and LD formation, though in some cases the LD-like structures do not stain for neutral lipid (7,30,31,37). Analysis of *Reep1-/-* mouse embryonic fibroblasts (MEFs) showed a dramatic alteration of ER organization (Supplementary Material, Fig. S5A and B), with a larger proportion of apparent sheet ER in *Reep1-/-* cells (Supplementary Material, Fig. S5B and C), in agreement with a previous study (17). Cell fractionation studies using *Reep1+/+* and *Reep1-/-* MEFs showed that Reep1 specifically localizes to ER, and there are no differences in mitochondrial complex I activity (Supplementary Material, Fig. S5D–F).

To investigate further any role for Reep1 in LD formation, we stained cerebral cortical sections for LDs using the Vala Sciences Lipid Droplet Screen-Certified Kit, and significant LD abnormalities were noted (Fig. 4B and C). We also investigated MEFs, which express low levels of Reep1 protein (Fig. 5A). Quantification of the fluorescence intensities of BODIPY 493 and LD540 staining were similar in *Reep1−/−* and *Reep+/+* cells, with a trend toward modest reduction in *Reep1-/-* cells (Fig. 5B and C). However, after cells were stimulated with oleic acid, a monounsaturated fatty acid that stimulates LD formation, staining intensities in *Reep1+/+* cells increased significantly, while they remained essentially unchanged in *Reep1−/−* cells (Fig. 5B and C and Supplementary Material, Fig. S5G). Upon differentiation of MEFs into adipocytes *Reep1+/+* cells form large LDs, while *Reep1-/-* cells do not (Fig. 5D). Together, these results establish a specific role for Reep1 in LD formation.

Interestingly, we observed that the number of LDs (Fig. 5E) is similar in *Reep1-/-* MEFs before and after treatment with oleic acid (as assessed using LD540), while the size of LDs is significantly reduced compared to the wild-type cells (Fig. 5F). In MEFs transfected with a Reep1 expression construct, the number of LDs increased in both *Reep1+/+* and *Reep1-/-* cells after treatment with oleic acid (Fig. 5E); recombinant Reep1 expression increased LD size in the *Reep1-/-* cells. These results suggest that Reep1 is involved in determining the size of LDs in cells, as previously reported for its binding partner atlastin-1 (30).

Reep1-/- cells have perilipin defects in LDs

There is an abnormal accumulation of TIP47, a member of the perilipin family, on the surface of LDs in *Reep1-/-* MEFs (Fig. 5G-I). Along these lines, we observed that levels of perilipin A, which coats LDs and is involved in regulating lipid stores, are decreased in *Reep1-/-* WAT (Fig. 6A). Furthermore, phosphorylation of perilipin was significantly increased in *Reep1-/-*tissue (Fig. 6B), which may trigger fragmentation and dispersion of LDs (38). This hypothesis was confirmed by treating MEFs with a specific inhibitor of protein kinase A (PKA)-dependent phosphorylation at perilipin Ser492, Rp-8-PIP-cAMPs, which restored oleic acid-mediated increases in LD size in *Reep1-/-* MEFs (Fig. 6C and D).

Reep1 and atlastin-1 in LD formation

To understand how absence of Reep1 can modify ER shaping and LD formation, we analysed its binding partner atlastin-1, a membrane-bound ER GTPase mutated in SPG3A (7). Recombinant atlastin-1 and Reep1 expressed in MEFs localize to ER tubules and, for Reep1 in particular, along bundled ER tubule-like structures (Supplementary Material, Fig. S6A), as

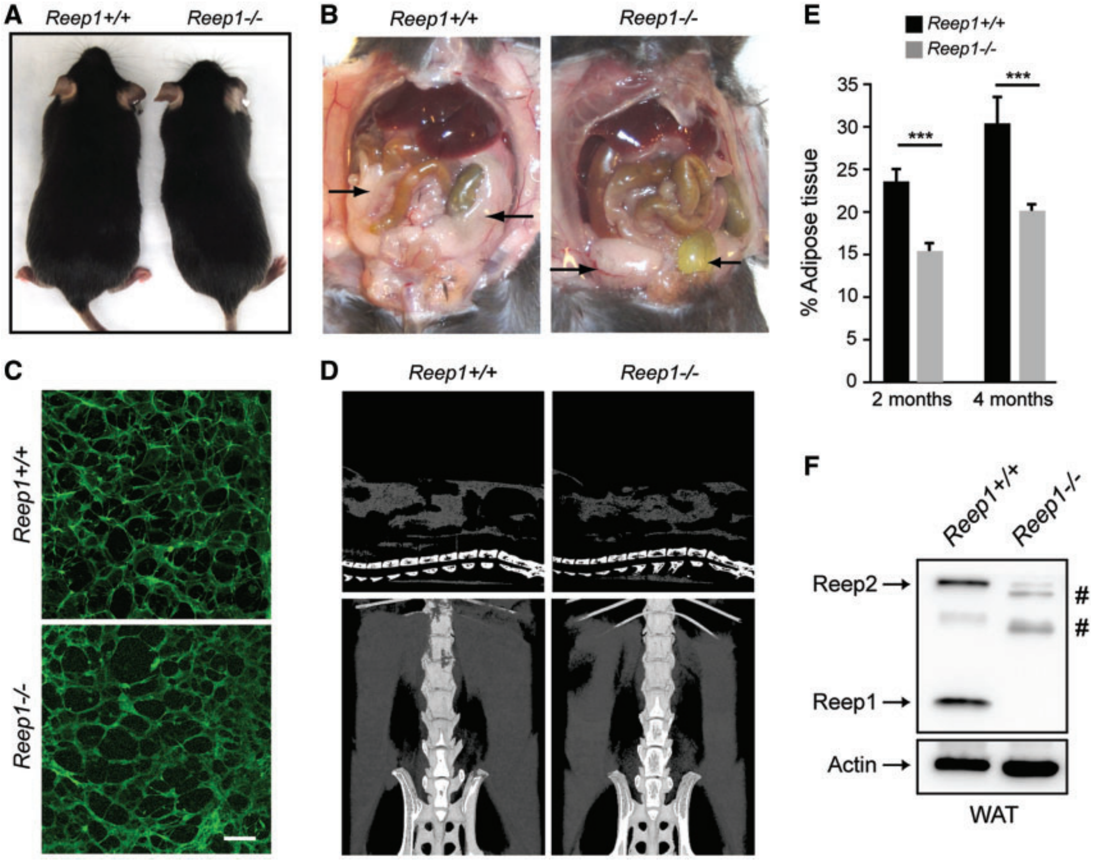

Figure 2. *Reep1* disruption causes lipodystrophy. (**A**) Representative photograph of *Reep1*+/+ and the thinner *Reep1*−/− mice. (**B**) Images showing a decrease in the abdominal white fat deposits (black arrows) in *Reep1*−/− mice. (**C**) Photos of sections of adipose tissue stained with BODIPY 594. Scale bar, 500 μm. (**D**) Representative images of CT scan analysis of total fat tissue in *Reep1*+/+ and *Reep1*−/− mice. (**E**) Volumes of fat tissue in *Reep1*+/+ and *Reep1*−/− mice quantified from CT scans as shown in **D** ($n = 10$ mice, means ± SEM, $^{***}P < 0.001$). (**F**) Immunoblot analysis of Reep1 and Reep2. Actin was monitored as a control for protein loading. WAT, white adipose tissue. #, non-specific bands.

described previously (7). In NIH-3T3 and COS7 cells, Reep1 and atlastin-1 co-overexpression can induce formation of large LDs, and this requires atlastin-1 GTPase activity (Supplementary Material, Fig. S6B). In addition, there is a massive recruitment of adipose differentiation-related protein (ADRP)/perilipin-2 to LDs in cells overexpressing both REEP1 and ADRP (Supplementary Material, Fig. S6C). Unexpectedly, in atlastin-1/REEP1 overexpressing COS7 cells, these proteins localize not only to rims surrounding LDs but also co-localize with the ER luminal protein calregulin (Supplementary Material, Fig. S6D), indicating that ER tubules may surround LDs, thus complicating clear interpretation of LD versus ER membrane protein localizations.

Interestingly, atlastin-1 protein levels are significantly decreased in *Reep1*-/- cells (Supplementary Material, Fig. S6E), consistent with a role for atlastin-1 in regulating LD size (30). Moreover, while expression of recombinant human REEP1 in MEFs rescued the *Reep1*-/- LD phenotype before and after treatment with oleic acid, expression of atlastin-1 or GTPase-defective atlastin-1 K80A did not restore normal LD formation (Fig. 7). These observations indicate that Reep1 is important for the formation of LDs and could mechanistically link atlastin-1 and Reep1.

Reep1 binds the SPG17/BSCL2 protein seipin

Finally, the SPG17/BSCL2 protein seipin that also localizes to ER is known to be involved in regulating LD formation and morphology. In fact, recombinant Myc-REEP1 and HA-seipin interact robustly, as assessed by co-immunoprecipitation studies in NIH-3T3 cells (Fig. 8A). Endogenous co-immunoprecipitation of CHAPS-solubilized mouse brain extracts did not reveal specific co-precipitation, though Reep1 robustly interacted with atlastin-1 under these conditions (Fig. 8B). Importantly, mouse brain extracts chemically cross-linked using dithiobis(succinimidyl propionate) (DSP) exhibited a clear interaction between endogenous Reep1 and atlastin-1 proteins, suggesting that the interaction might be transient (Fig. 8C). Additional supportive experiments in COS7 cells show that recombinant Reep1 co-localizes closely with wild-type seipin and two well-described, pathological seipin SPG17 missense mutant proteins (Fig. 8D).

Discussion

Most cases of pure HSP result from autosomal dominant mutations in genes for SPG4, SPG3A, or SPG31 (2). Recently, *Reep1*–/– mice were generated (17), and these animals developed hind limb dysfunction with weakness, spasticity and degeneration of axons of the corticospinal tract. *Reep1*–/– cells also had defects in ER structure (17). The *Reep1*-/- mice described here similarly recapitulate many aspects of human SPG31, with neurophysiologic studies showing the physiologic basis for the spasticity. Thus, our results suggest that *Reep1*-/- mouse spasticity results from increased motoneuron responsiveness, possibly in the

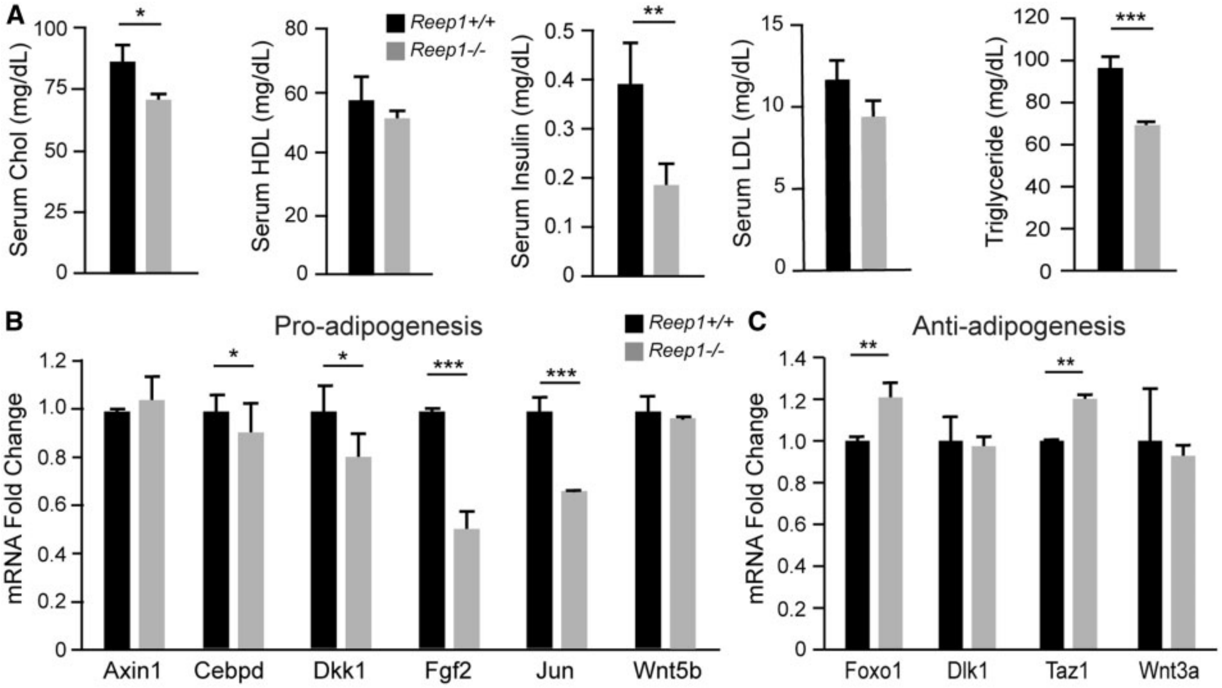

Figure 3. Altered serum lipid parameters in *Reep1*-/- mice. (**A**) Serum triglycerides, cholesterol, and insulin are decreased in *Reep1*−/− mice. Chol, cholesterol; HDL, high-density lipoprotein; LDL, low-density lipoprotein. (**B–C**) Quantitative qRT-PCR analysis of pro- (**B**) and anti- (**C**) adipogenesis mRNAs using the Qiagen Mouse Adipogenesis PCR Array. Graphs show means ± SEM ($n = 3$ mice, each in triplicate). $^{*}P < 0.05$, $^{**}P < 0.01$, $^{***}P < 0.001$.

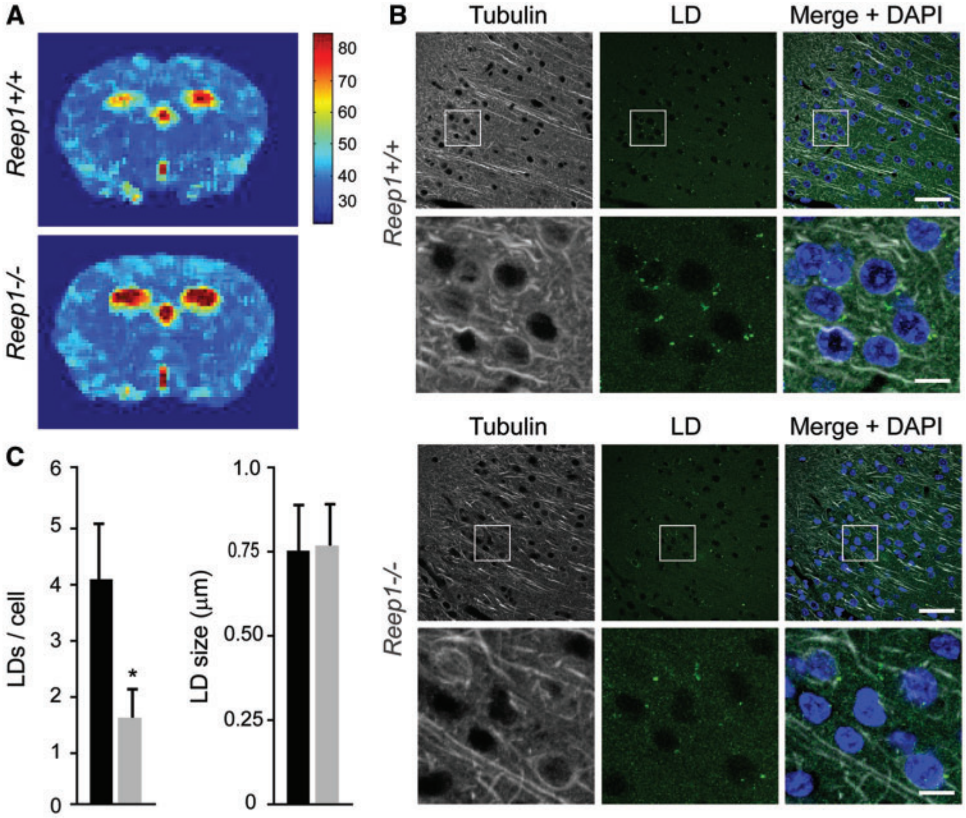

Figure 4. LD alterations in *Reep1*-/- mouse cerebral cortex. (A) Representative T_2 relaxation time map (additional details in Supplementary Material, Fig. S4D and E) for *Reep1*+/+ and *Reep1*−/− brain. The pixel intensity of the T_2 maps represents the quantitative T_2 values (in ms scale bar to the right). (**B**) Cortical sections of *Reep1*+/+ and *Reep1*−/− mice stained for tubulin (gray), LDs (Vala; green) and DAPI (blue). Boxed regions are enlarged below. Scale bar, 100 μm. (**C**) Quantification of number and size of LDs in cell bodies of neurons from sections as in **B** ($n = 3$ mice, means ± SEM). $^{*}P < 0.05$.

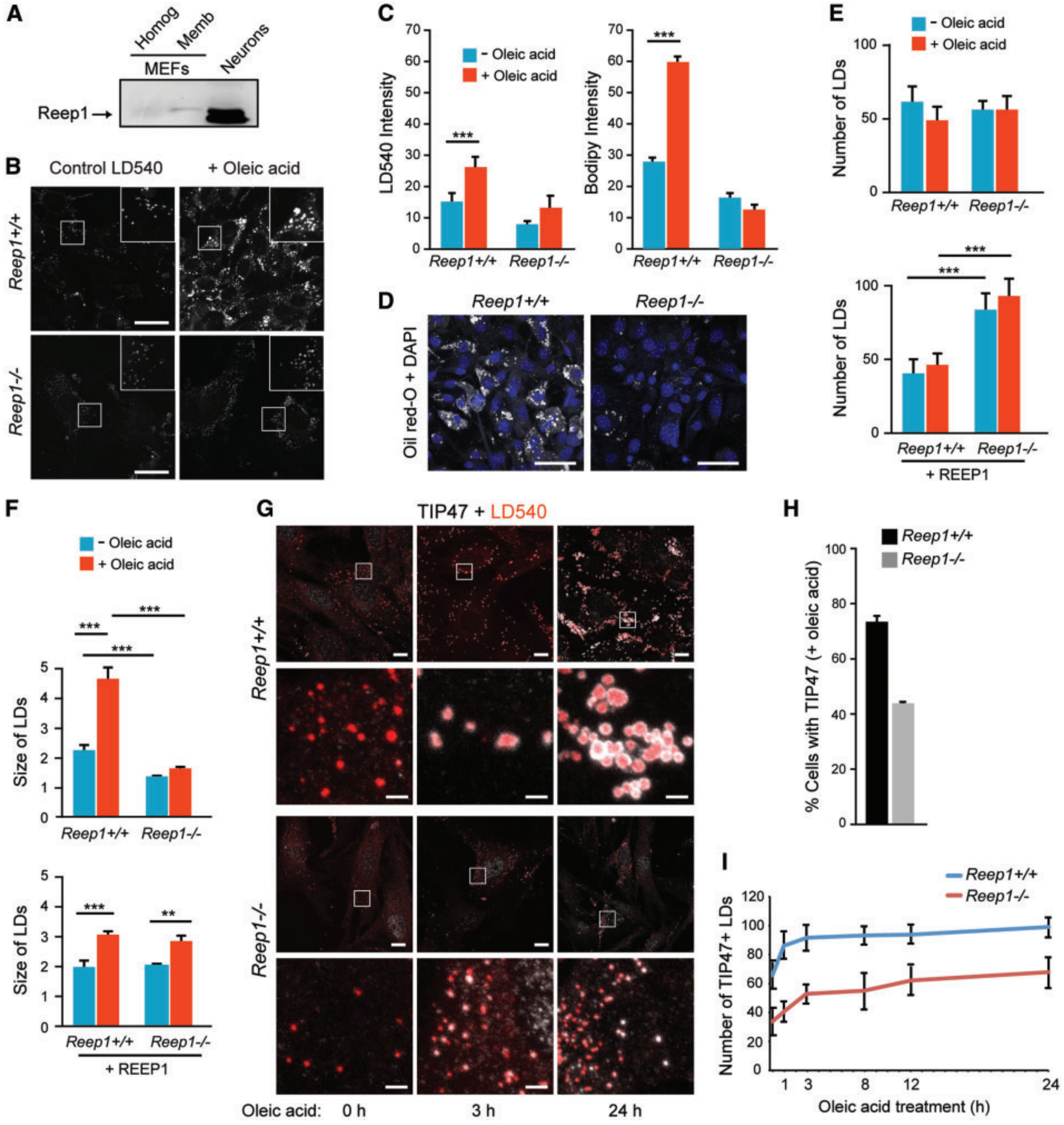

Figure 5. LD abnormalities in *Reep1*-/- mice. (**A**) Immunoblot analysis of endogenous Reep1 protein expression in *Reep1*+/+ neurons and MEFs in total homogenates (Homog) and membrane fraction (Memb). (**B**) LD540 staining of MEFs from *Reep1*+/+ and *Reep1*−/− mice before and after treatment with oleic acid. Boxed regions are enlarged in the upper right hand-corner insets. Scale bars, 10 μm. (**C**) Graphical representation of total LD540 and BODIPY 594 staining intensities in *Reep1*+/+ and *Reep1*−/− MEFs before and after treatment with oleic acid (means ± SEM; $n = 60$). ***$P < 0.001$. (**D**) Impairment of MEF differentiation. MEFs from *Reep1*+/+ and *Reep1*-/- mice were cultured and differentiated into adipocytes. Oil red O staining of LDs with DAPI (blue) staining nuclear is shown. Scale bar, 10 μm. (**E-F**) Quantification of number (**E**) and size (**F**) of LDs in MEF cells transfected (+REEP1) or not with a REEP1 expression construct and treated (red) or not (blue) with oleic acid. **$P < 0.01$, ***$P < 0.001$. (**G-H**) Quantification of cells (as in **C**) with TIP47^+ LDs in *Reep1*+/+ and *Reep1*−/− MEFs after treatment with oleic acid for the indicated times. Boxed regions are enlarged directly below. Scale bar, 20 μm. (**I**) Quantification of cells with TIP47^+ LDs at several time points after oleic acid treatment. $P < 0.001$.

setting of higher levels of the neurotransmitter glutamate. In fact, several groups have already shown that glutamate release can maintain and amplify the ongoing activity of motoneurons, contributing to clinical signs of spasticity and rigidity (39,40).

Another key finding here is that Reep1 is also expressed in WAT, albeit at low levels, and that Reep1 depletion causes lipoatrophy, with significantly decreased visceral fat. Furthermore, *Reep1*-/- MEFs exhibit a clear and significant impairment of differentiation into adipocytes and LD size. Our data further show that the Reep1 deletion modifies perilipin phosphorylation in MEFs. Earlier studies have shown that phosphorylation of perilipin is critical for triglycerol storage and hydrolysis by regulating LD formation and degradation by autophagy (41,42). More recently, it has been demonstrated that PKA mediates Ser492 phosphorylation of mouse perilipin (equivalent to Ser497 in

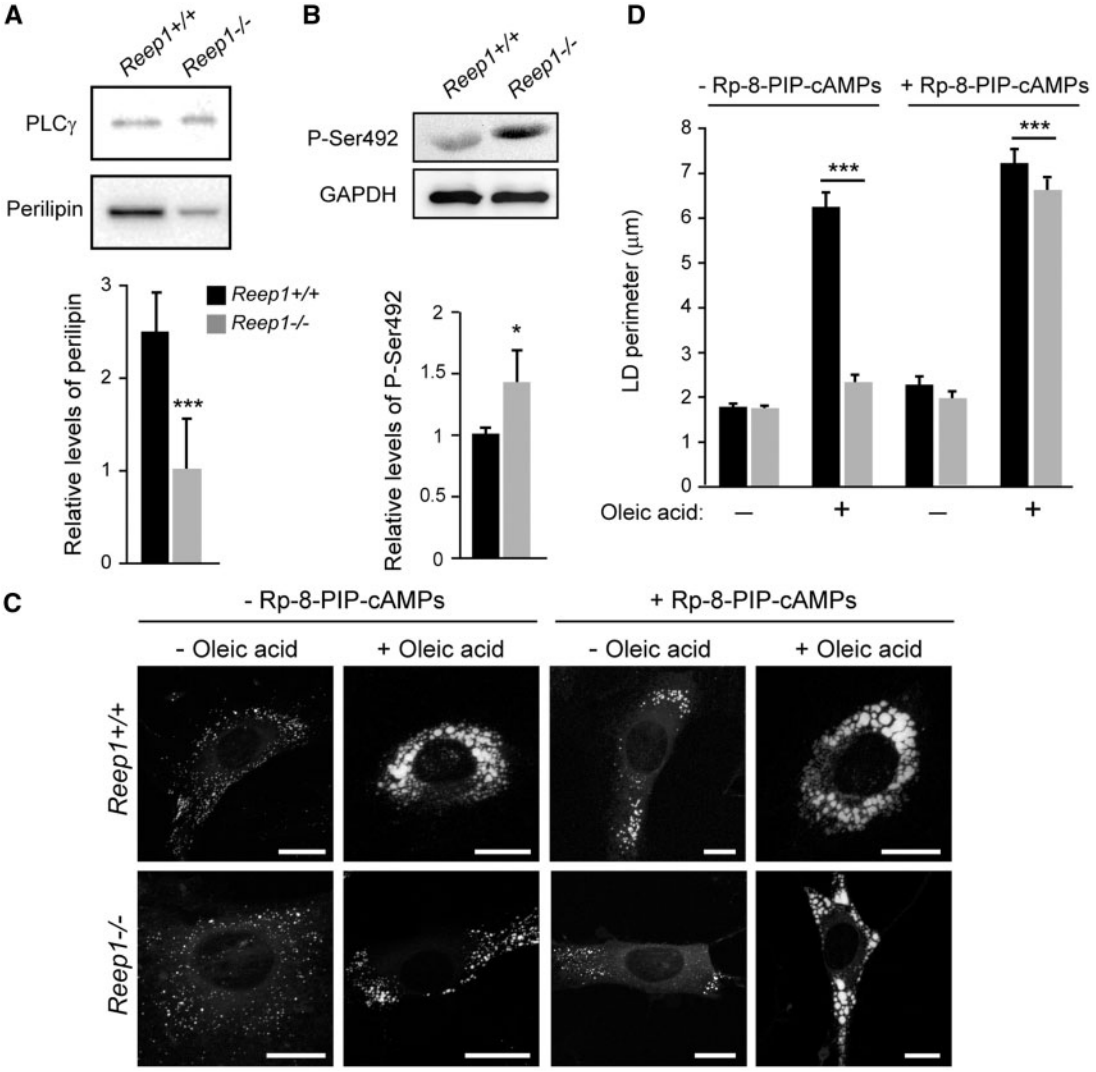

Figure 6. Increased phosphorylation of perilipin in *Reep1*-/- cells. (**A**) Immunoblots of perilipin in total MEF lysates from *Reep1*+/+ and *Reep1*−/− mice (~2.5 and 0.8 relative expression levels, respectively). PLCγ levels were monitored as a control for protein loading. (**B**) Phosphorylation defect of perilipin in the *Reep1*-/- MEFs. (**C**) *Reep1*+/+ and *Reep1*-/-MEFs were incubated with a site-selective lipophilic PKA inhibitor (Rp-8-PIP-cAMPS) in presence or absence of oleic acid. *Reep1*+/+ and *Reep1*-/cells show a high accumulation of LDs after inhibitor treatment, suggesting a perilipin phosphorylation defect in *Reep1*-/- mice. (**D**) Quantification of LD perimeters from **C** (means ± SEM; $n = 60$). $^{***}P < 0.001$. Scale bars, 10 μm.

human perilipin), driving fragmentation and dispersion of LDs (38). In our experiments, incubation of *Reep1*-/- MEFs with a specific PKA inhibitor increased the formation of large LDs in wild-type cells and, importantly, rescued the LD phenotype in *Reep1*-/- cells. Along these lines, overexpression of REEP1 in COS7 cells caused a significant enrichment of ADRP/perilipin 2 at LDs.

Though Reep1 appears to play an important role in LD formation, *Reep1*-/- mice still accumulate some adipose tissue, and *Reep1*-/- MEFs still produce LDs. This is not surprising, since there are at least three other closely-related Reep proteins, Reep2-4, in mice. However, LD quantity (and size in some cell types) is significantly decreased, suggesting that any redundancy is not complete.

Interestingly, the Fsp27 protein localizes to LDs and promotes lipid storage in adipocytes, and while the WAT volume of Fsp27 null mice is unchanged from wild-type (43), the visceral ratio of total volume WAT to mass in *Fsp27*−/− mice is lower (44). Histological analysis of WAT indicated that adipocytes in *Fsp27*−/−mice have multiple small LDs, but adipocyte size is not decreased. Another related study showed that FIT2 (Fat storage-Inducing Transmembrane protein 2) regulates LD formation (45). FIT2 is a 6-transmembrane domain-containing protein whose conformation likely regulates its activity in modelling the ER and mediating LD formation. The authors suggested that FIT2 is regulated by conformational changes induced by ER membrane lipids or interactions with other ER proteins. It is tempting to speculate that atlastin-1 activity may be similarly regulated by its interaction with Reep1, and in fact this type of regulation has been well characterized for other proteins such as HMG-CoA reductase (46).

Recent studies have revealed important roles of the SPG17/BSCL2 protein seipin, which localizes to the ER, in lipid storage at both the cellular (LDs) and whole-body (adipose tissue development) levels (47,48). We show that REEP1 can interact with seipin, which is highly expressed in adipose tissue and strongly induced during adipocyte differentiation (49–51). Modelling loss-of-function seipin mutations in Berardinelli-

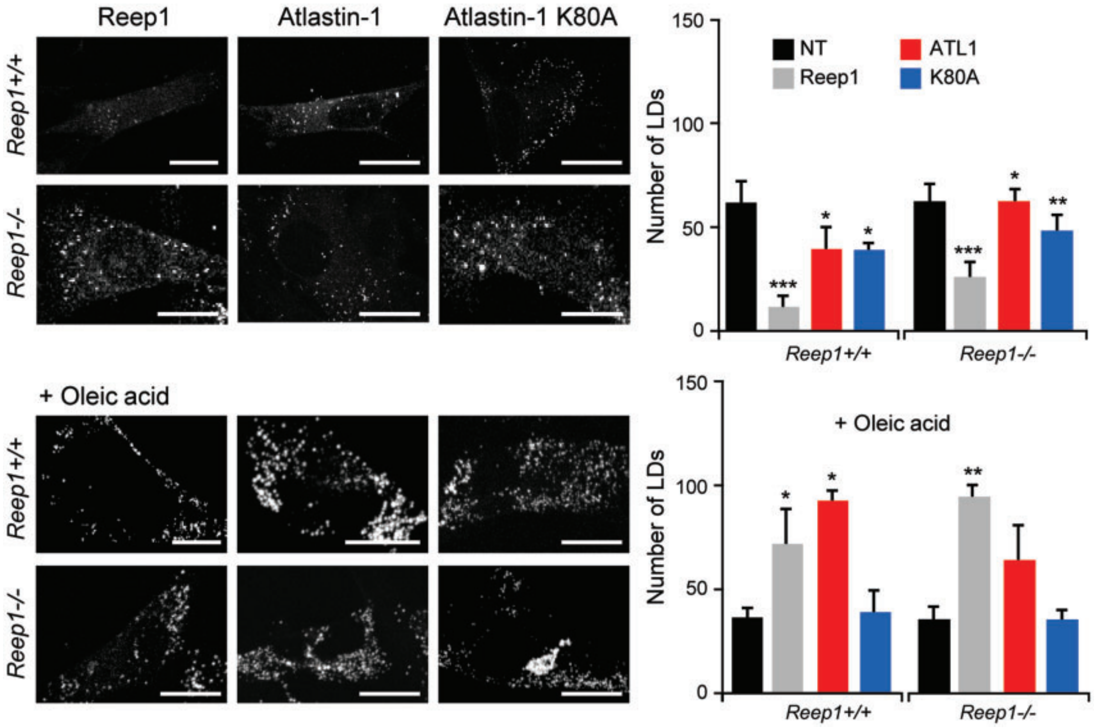

Figure 7. LD540 staining of *Reep1*+/+ and *Reep1*−/− MEFs transfected with Reep1, atlastin-1, or atlastin-1 K80A constructs as indicated. Graphs represent the quantification of cells before and after treatment with oleic acid (means ± SEM; $n = 50$). *$P < 0.05$, **$P < 0.01$, ***$P < 0.001$. Scale bars, 10 μm.

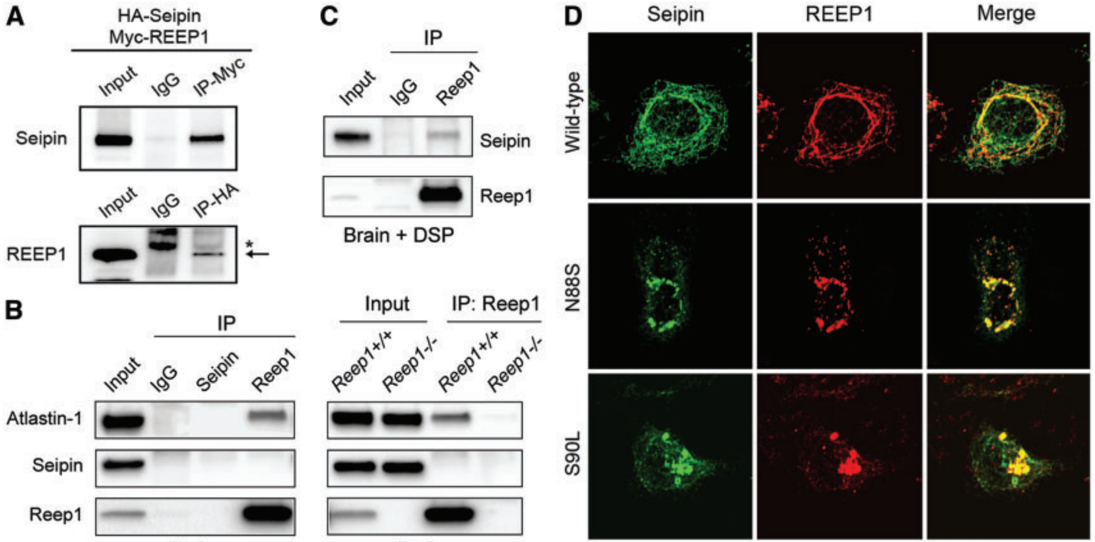

Figure 8. SPG17 protein seipin interacts with REEP1. (**A**) NIH-3T3 cells were co-transfected with Myc-REEP1 and HA-seipin constructs. Cell lysates were immunoprecipitated with anti-Myc and anti-HA antibodies and immunoblotted for HA (for seipin) and Myc (for REEP1) epitopes as indicated. (**B**) Mouse brain extracts from the indicated genotypes were immunoprecipitated (IP) as indicated and then immunoblotted for atlasitn-1, seipin, and Reep1. Panels on the left used *Reep1*+/+ extracts. (**C**) Imunoprecipitations (IP) were carried out as in **B**, except that extracts were first subjected to cross-linking with DSP, which is then cleaved in SDS-PAGE sample buffer. (**D**) Distribution of HA-seipin (green) and Reep1 (red) constructs after co-transfection in COS7 cells. Scale bar, 10 μm.

Seip congenital lipodystrophy, *Bscl2-/-* mice have prominent lipodystrophy (52–54). However, though lipoatrophic, these mice exhibit residual fat pads, for which histological analysis shows immature adipocytes, with a defect in the LD development (52,53). Furthermore, *Bscl2-/-* MEFs show impairment of adipocyte differentiation (49). Studies performed in yeast and human non-adipose cells have shown that *Fld1* and *Bscl2* null mutations, respectively, alter LD morphology, with formation of giant LDs or clustering of numerous tiny droplets (48,55). *Reep1-/-* mice exhibit a similar phenotype, with reduction of WAT volume and disruptions in LD morphology. The similarities among these mutant mice combined with the interaction between Reep1 and seipin indicate that these proteins could function together in LD formation.

LD formation and size are highly regulated, and atlastins function in regulating LD size (30). Atlastin GTPase activity is known to mediate the formation of the tubular ER network through interactions with proteins of the reticulon and Yop1p/DP1/REEP superfamilies (7,9,56). Co-transfection of Reep1 and atlastin-1 causes the formation of large and numerous LDs in COS7 cells. Several studies have already shown that ER proteins including reticulons and REEPs have curvature-promoting properties through hydrophobic hairpin domains and scaffolding (10–12,24). We suggest that REEP1 and atlastin-1 cooperate to regulate LD size, though mechanisms still remain unclear.

LD biogenesis is also facilitated by the special structures of some ER proteins. One model for LD formation emphasizes the physical properties of lipid emulsion as well as the impact of curvature induced by ER proteins (57). The authors suggested that two cytosolic populations of LDs exist, smaller and expanding LDs. Smaller LDs bud from ER and are characterized by the presence of diacylglycerol *O*-acyltransferase 1 (DGAT1). The expanding LDs require the accumulation and the activity of glycerol-3-phosphate acyltransferase 4 (GPAT4)-DGAT2, which enhances the synthesis of triacylglycerol. Finally, they suggested that proteins such as seipin and FIT2 influence the surface tension and the budding process during LD formation from the bilayer ER-membranes (57).

Surface tension is critical for the formation and release of LDs (57), and we speculate that recruitment of Reep1 and atlastin-1 to sites of formation of the expanding LD induces negative curvature of the ER membrane; atlastin-1 then can form *trans* interactions necessary for membrane fusion. This could explain the observation of smaller LDs in *Reep1-/-* cells. *Reep1-/-* cells could also have defective DGAT2 accumulation in LDs, which inhibits accumulation of triglycerides and influences LD size.

The decrease in LD number but not size in neurons of *Reep1-/-* cerebral cortex is seemingly at odds with the alterations in LD size observed in MEFs. This could be for a number of reasons, including technical factors (e.g., inability to assess accurately smaller LDs in these brain sections) or else differential interactions of Reep1 across different cell types. Finally, Reep1-4 proteins may function similarly, and the relative contribution of Reep1 in the brain (which has high Reep1 levels) to Reep1-4 dosage likely differs from the contribution of Reep1 to Reep1-4 dosage in peripheral tissues (where Reep1 levels are much lower, even accounting for effects of Reep1 depletion on Reep2 stability that we observed in WAT). A better mechanistic understanding of the roles of Reep1 in LD biology should clarify this in the future.

Our study thus provides a new model for HSP and exposes a link between regulation of LD formation and morphology by Reep1 via interactions with atlastin-1 and seipin, with dysregulation possibly contributing to axonal dysfunction in long corticospinal neurons. In addition, Reep1 has been shown to promote ER stress resistance in *Drosophila*, and it also prevents Tau-mediated degeneration *in vivo* by inhibiting the formation or accumulation of thioflavin-S-positive Tau clusters (58). These observations combined with our results supports the idea that neuronal degeneration in HSP patients results from functional ER changes with consequences for LD formation, metabolism of Tau, ER stress, and ER shaping – all of which are vital in the structural organization of the CNS.

Materials and Methods

Generation and breeding of *Reep1-/-* mice

All animal experiments were approved by the NINDS/NIDCD Animal Care and Use Committee in Bethesda, Maryland. *Reep1-/-* mice on a 129/SvEv x C57BL/6 background, produced by homologous recombination-based gene targeting from the gene trap clone OST398247 (Supplementary Material, Fig. S1A), were purchased from the Texas A&M Institute for Genomic Medicine. For construction of the targeting vector, the mouse chromosome 6 sequence (nucleotide #71,623,408-71,745,067) was used as a reference. The heterozygous mice produced were then backcrossed for at least 10 generations into the C57BL/6J background. For subsequent breeding, one male and one female at sexual maturity were housed in the same cage. After gestation and delivery, P1 pups were sacrificed to generate neuronal cell cultures or else the young mice were weaned 21–28 days after birth for other studies. For genotyping, genomic DNA was isolated from tail snips using standard procedures. Gene-specific PCR was carried out with Taq DNA polymerase (Invitrogen) and primers specific for *Reep1* (forward: 5′-ACGC TACAGACCCATGGGTAGC-3′), Neo cassette (reverse: 5′-ATAAA CCCTCTTGCAGTTGCATC-3′), and genomic reverse (5′-CCAAGG CATTTTCTTCCAAAGG-3′) (Supplementary Material, Fig. S1B).

Anatomic and histologic analyses

Mice were transcardially perfused with 4% paraformaldehyde (PFA) or 2% PFA/2% glutaraldehyde. Brain and spinal cord were then excised and post-fixed in 4% PFA or 2% PFA/2% glutaraldehyde, respectively, for 16 h. Sections (50 μm thick) were cut with a Leica CM3050S cryostat and stained with H & E, Nissl, Luxol fast blue or Cresyl violet, or else immunostained as described (59). For measurement of axon size in the spinal cord, sections (1 μm thick) were cut with a PELCO easiSlicer (Ted Pella), and then transferred to a drop of distilled water on a glass slide. Sections were dried on a slide warmer, then covered with a drop of toluidine blue for 1 min. Next, sections were gently rinsed with distilled water and dried. For fat tissue preparation, abdominal white fat was dissected from the mice and stored at -80 °C. Thick sections (50 μm) were prepared using a cryostat at -50 °C, then fixed with 4% formaldehyde and stained with H & E or BODIPY 493. Images were acquired using a LSM710 laser scanning microscope (Carl Zeiss Microscopy) and analysed using ImageJ software (NIH).

Behavioural studies

Mice ($n \geq 10$) of ages 2 and 4 months were compared in two different trials. Observers were blind to their genetic status during testing. To assess motor function, mice were tested using a Rotarod apparatus (MedAssociates ENV-575M 5 Station Rotarod Treadmill) as previously published (59). Grip strength was monitored quantitatively in these same mice using a grip strength meter (Bioseb) (39). Analysis of gait was performed with the TreadScan apparatus and software (CleverSys). Videos of gait during treadmill locomotion were captured, and frame-by-frame measures of mouse walking patterns were acquired at a constant running speed of 14 cm/s. According to the manufacturer, TreadScan generates measures of stride length and width as well as fore and rear foot-placement rotation-angle during movement (with degrees relative to the body midline). It also computes stance time (including stationary time), propel time (latter portion of stance when the paw is propelling the body), swing and break time (early part of stance until the paw reaches maximum contact).

Tissue preparation and immunoblotting

Preparation of cell extracts, gel electrophoresis and immunoblotting were performed as described previously (13,56). Protein concentrations were determined using Pierce BCA Protein Assay Reagent (Life Technologies). For immunoblotting, proteins were resolved by SDS-PAGE and membranes were incubated with antibodies (1–5 μg/ml) overnight at 4˚C.

For whole tissue lysate preparation, mice were dissected and tissues were weighed. Briefly, fresh cold lysis buffer (150 mM NaCl; 50 mM Tris HCl, pH 7.4; 1 mM EDTA; 1% NP40; 0.5% deoxycholate; 0.1% SDS; 1× Roche Complete Protease Inhibitor; 1 mM PMSF) was added to each tissue sample, then homogenized and sonicated. Samples were spun down twice in a 4˚C refrigerated centrifuge at 13,000 *g* for 30 min. The supernatant was retained and proteins quantified; 20–30 μg of the sample was evaluated by immunoblotting following SDS-PAGE. For immunoprecipitation experiments, brains from 2-month old mice were lysed in PBS with 1% CHAPS and 1× Roche Complete Protease Inhibitor. Where indicated DSP was added to a final concentration of 1.5 mM for 60 min on ice before the reaction was quenched with 1 M Tris (pH 7.5). NIH-3T3 and COS7 cells were maintained under standard conditions, and DNA vector transfections were performed with Avalanche-Omni Transfection Reagent (EZ Biosystems) for 24 h. Immunoprecipitations were conducted as described previously using protein A/G PLUS-agarose beads (Santa Cruz Biotechnology) (7).

For adipose tissue isolation, mice were dissected at 2 months of age, and tissue was weighed. After rinsing once with cold 1× PBS, immediately 1:5–1:10 (w/v) tissue to buffer of fresh cold lysis buffer (150 mM NaCl; 50 mM Tris HCl, pH 7.4; 1 mM EDTA; 1% NP-40; 0.5% deoxycholate; 0.8% SDS; 1× Roche Complete Protease Inhibitor; 1 mM PMSF) was added. Signal quantifications were carried out with Image Lab Software (BioRad) and normalized on the actin loading control signal.

Cortical neuron cultures

Primary cultures of mouse cerebral cortical neurons were prepared from P1 mice, plated at a density of ~1.0 x 10^4/cm^2 on coverslips, and maintained and immunostained as described previously (59). Briefly, brain tissue was subjected to papain digestion (5 U/ml, Worthington) for 45 min at 37 °C. The digested tissue was carefully triturated into single cells then centrifuged at 1000 rpm for 5 min and resuspended in warm Neurobasal Medium supplemented with 10% heat-inactivated FBS, 1× B27 (Gibco), 1× GlutaMAX, 0.45% D-glucose (Sigma-Aldrich) and penicillin/streptomycin (Gibco 15140-122). Dissociated cells were plated onto dishes or coverslips pre-coated with poly-D-lysine (BD Biosciences) and maintained at 37 °C in a 5% CO_2 humidified incubator.

Preparation of MEFs

Pregnant mice at day 14 post coitum were sacrificed and the uterine horns dissected. Each embryo was separated from its placenta, and brain and dark red organs were excised. After washing with fresh PBS, embryonic tissues were minced and suspended in trypsin-EDTA, then incubated with gentle shaking at 37 ˚C for 15 min. After addition of 2 volumes of fresh MEF medium [DMEM (high glucose, Gibco 41966-052), 10% (v/v) FBS, 1:100 (v/v) L-glutamine (200 mM; Gibco 25030-024) and 1:100 (v/v) penicillin/streptomycin (Gibco 15140-122)], remaining tissue pieces were removed, and the supernatant was spun down (5 min, 1000 *g*). The cell pellet was resuspended in MEF medium and plated (59).

MEF and neuronal transfections

MEFs and neurons were cultured in DMEM supplemented with 10% FBS and Neurobasal Medium supplemented with 10% heat-inactivated FBS, B27 (Gibco), GlutaMAX, 0.45% D-glucose (Sigma-Aldrich) and penicillin/streptomycin (Gibco 15140-122) at 37 °C in a 5% CO_2 humidified incubator, respectively. DNA transfections were performed using Avalanche-Omni Transfection Reagent (EZ Biosystems) for 1 (MEFs) or 6 (neurons) days, following the instructions of the manufacturer. Eukaryotic expression constructs for HA-atlastin-1, HA-atlastin-1 K80A, HA-Reep1 and untagged Reep1 have been described (7,13). Quantifications of fluorescence intensity and measure of axon size and branching were carried out with ImageJ and NeuronJ (NIH), respectively.

Mouse CT imaging

In vivo CT studies were conducted under an animal study protocol approved by the NIH NINDS/NIDCD Animal Care and Use Committee. Animals were maintained under general anaesthesia (1–2% isoflurane delivered by a gas mixture of oxygen, nitrogen, medical air) administered via nosecone, and they were placed in a secure anatomic position that restricted motion and allowed for constant respiratory monitoring. Mouse anatomical CT was performed on a Bruker SkyScan1176 micro-CT scanner (Bruker) with the X-ray source (energy range 20–90 kV) biased with 50 kV/500 μA, using an AI 0.5 mm filter to reduce beam hardening. The integrated scanner heater was used to maintain body temperature. Images were acquired with a pixel size of 36.13 μm; camera-to-source distance was 170 mm, and object-to-source distance of 123 mm. Projections (360) were acquired with an angular resolution of 0.5° over a 180° rotation. Two frames were averaged for each projection, with an exposure time of 55 ms per frame. Scan duration was approximately 20 min. Tomographic images were reconstructed using vendor-supplied software based on the Feldkamp cone beam algorithm. After scanning, images were reconstructed and processed. Reconstruction was performed using NRecon software (Bruker MicroCT) with an isotropic pixel size of 36.13 μm. To remove noise and clarify areas of fat from surrounding soft tissue, software-specific artefact reductions were utilized (smoothing factor of 3, ring artefact correction of 8 and beam hardening correction of 30%). The contrast range provided an adequate window for fat tissue with saturation of bone (allowing the air and soft tissue window to encompass the majority of the greyscale range). For post-processing, Bruker CT-Analyser was used to select the volume of interest (VOI), which began at the first thoracic vertebrae and terminated at the midsection of femoral heads in the hip joint. Upon visual inspection of cross-sections within the VOI, grayscale values of each animal's fat window were determined; a threshold was applied to create a mask of fat within the VOI. A larger threshold was used to create a mask of the entire body volume. These masks were then compared to yield the percentage of fat versus body volume over the VOI.

Antibodies and dyes

Mouse monoclonal antibodies were used against β-tubulin (IgG_1, clone D66, Sigma-Aldrich), neuronal β-tubulin (14944302; Covance), actin (clone AC40; Sigma-Aldrich), PLCγ1 (2822; Cell

Signalling), HA-epitope (ab9110; Abcam), and Myc-epitope (IgG_1, clone 9E10; Santa Cruz Biotechnology). Rabbit polyclonal antibodies were used against perilipin (34705; Cell Signalling), anti-P-perilipin 1-serine 497 antibody (4855; Vala Sciences), myelin (ab30490; Abcam), BSCL2/seipin (106793; Abcam), Reep1 (17988-1-AP; Proteintech), Reep2 (15684-1-AP; Proteintech), Reep5 (14643-1-AP; Proteintech), calreticulin (ab2907; Abcam), calregulin (Clone T19; Santa Cruz Biotechnology), AIF (Clone E20; Epitomics), VDAC (ab15895; Abcam), HA-probe (Y-11; Santa Cruz Biotechnology) and an affinity-purified atlastin-1 antibody (56). BODIPY 493 and BODIPY 594 dyes were obtained from Invitrogen, and LD540 was a gift from Prof. Christoph Thiele (60).

Confocal immunofluorescence microscopy

To observe the ER and the cytoskeleton, cells plated on coverslips were fixed for 20 min with 4% formaldehyde or 5 min with methanol, respectively. Then cells were blocked for 30 min with 10% goat serum, 0.1% Triton X-100 in PBS (pH 7.4) at room temperature. After three washes, coverslips were incubated with primary antibodies diluted in 1% goat serum. Alexa Fluor anti-rabbit and anti-mouse secondary antibodies (Invitrogen) were used at 1:400. Cells were counterstained with 4',6-diamidino-2-phenylindole (DAPI; 0.1 mg/ml) where indicated and mounted using Fluoromount-G (SouthernBiotech). The cells were imaged using a Zeiss LSM710 confocal microscope with a 63× 1.4 NA Plan-Apochromat oil differential interference contrast objective, and image acquisition was performed using Zen software (Carl Zeiss Microscopy). Images were processed with ImageJ, Adobe Photoshop 7.0 and Adobe Illustrator CC software.

Oleic acid treatment and staining of MEFs

To analyse LDs, MEFs were cultured as described above and incubated with 200 μM oleic acid (Sigma-Aldrich), as described previously (56). After overnight incubation, cells were fixed, permeabilized, and immunostained with antibodies then incubated with a solution of 0.1 μg/ml LD540 for 5 min or else BODIPY 493 or 594 (Invitrogen) in PBS overnight. Then cells were washed and mounted in Fluoromount-G (SouthernBiotech). Fluorescence images were acquired with a 63× objective as a series of the optical z-stacks spanning the entire cell, using the transmitted light of a Zeiss LSM710 laser scanning confocal microscope (Carl Zeiss Microimaging). Recording conditions were set to obtain a fluorescence signal below saturation levels. Cell boundaries were defined by applying a threshold to each of the z-sections. The proportion of fluorescence was calculated using ImageJ. Typically, 300 cells in three different experiments were randomly selected and examined for each condition.

Electrophysiology

Experiments were performed on 2-to-4 day-old mice. Mice were decapitated and eviscerated, then placed in a dissecting chamber and continuously perfused with artificial cerebrospinal fluid (concentrations in mM): 128.35 NaCl, 4 KCl, 1.5 $CaCl_2.H_2O$, 1 $MgSO_4.7H_2O$, 0.58 $NaH_2PO_4.H_2O$, 21 $NaHCO_3$, 30 D-glucose) bubbled with 95% O_2 and 5% CO_2. After a ventral laminectomy, the spinal cord was isolated together with attached roots and ganglia and maintained at room temperature. Motoneuron extracellular activity was recorded with plastic suction electrodes into which individual ventral roots were drawn. Recordings were obtained from the L1 (left and right) and L5 (left or right) ventral roots. Locomotor-like activity was elicited by stimulating a sacral (S3 or S4) dorsal root ganglion (4 Hz, duration: 10 s, the duration of each stimulus: 250 μs). The lowest intensity at which the train elicited locomotor-like activity was defined as the threshold. Frequencies were measured from two trials at 2, 5 and 10× thresholds.

Monosynaptic reflex responses recorded from L5 ventral root were evoked by a single electrical stimulus to the ipsilateral L5 lumbar dorsal root or ganglion (stimulus duration: 250 μs). We measured the latency of the response as the time between the beginning of the stimulus artefact and the start of the response (i.e., when the inflection in the signal reaches 10 times the size of the pre-stimulus noise). We measured the responses for 2× and 10× thresholds. The stimulus threshold was defined as the current at which the minimal evoked response was recorded.

We used whole-cell current clamp to record motoneurons in vitro. Whole-cell recordings were obtained with patch electrodes (resistance: 6-10 MΩ) lowered blindly into the ventral horn of the spinal cord. Patch electrodes were filled with intracellular solution containing (in mM) 10 NaCl, 130 K-Gluconate, 10 HEPES, 11 EGTA, 1 $MgCl_2$, 0.1 $CaCl_2$ and 1 Na_2ATP, with pH adjusted to 7.2–7.4 with KOH. Motoneurons were only considered for subsequent analysis if they exhibited a stable resting membrane potential of -50 mV or more and an overshooting antidromically-evoked action potential. Input resistance was calculated from the slope of the current/voltage plot within the linear range. The liquid junction potential was not corrected. We recorded monosynaptic reflexes intracellularly in motoneurons. The threshold was determined independently for each neuron as the intensity that triggers an action potential in the recorded neuron.

Tracings

L5 ventral and dorsal roots were placed inside suction electrodes and backfilled with Cascade Blue dextran or Texas Red dextran for 12 h at room temperature (30–40 mM; 10,000 MW, Invitrogen) (61). Segments were then fixed for 24 h in 4% PFA at room temperature and then washed. They were then embedded in warm 5% Agar and transverse sections (100 μm) were cut on a vibratome (Leica, V1000). Sections were mounted on slides and cover-slipped with a solution made of glycerol and PBS (3:7). Images were acquired using a Carl Zeiss LSM710 confocal microscope with a 10× objective.

Polymerase chain reaction

Gene expression of Reep1 and Reep2 were analysed using the RapidScan kit (OriGene) following the instructions of the manufacturer. Primers were: Reep1, forward: 5′-CAAGGCTGTGAAG TCCAAGG-3′, reverse: 5′-GGCACTCTCAGAAGCACTCC-3′; Reep2, forward: 5′-GGATCATCTCTCGCCTGGTG-3′, reverse: 5'-TTAGGG CAGGCTCATCTCCT-3'. For real-time PCR, total RNA was extracted from white adipocyte tissue with TRIzol reagent (Invitrogen) according to the manufacturer's protocol. Reverse transcription of total RNA with $Oligo(dT)_{20}$ (Invitrogen) was performed using ThermoScript RT-PCR System (Invitrogen). Quantitative real-time PCR was carried out using an Applied Biosystems SYBR green PCR Master Mix 7900HT. The following thermal cycling program was applied: 10 min at 95 °C, 40 cycles of 15 s at 95 °C, 30 s at 60 °C and 1 min at 72 °C. Data were normalized to GAPDH expression levels using the comparative threshold cycle method.

MRI analysis

Animal study protocols to conduct MRI and MR spectroscopy studies were approved by the NINDS/NIDCD Animal Care and Use Committee. Age- and sex-matched *Reep1*-/- mice and their wild-type littermates ($n = 4$–5) were anaesthetized with 1.5% isoflurane, and then positioned in a stereotactic holder. Core body temperature was maintained at 37 °C using circulating water pad and monitored throughout the procedure. MRI was performed on a 7T, 21 cm horizontal Bruker Avance scanner with the brain centered in a 72 vol (transmit)/25 mm surface (receive) radio frequency coil ensemble to excite and detect the MR signal. A pilot scan, depicting gross brain anatomy in three mutually perpendicular directions, was acquired which in turn was used to obtain MR images and MR spectra. Quantitative, spin-spin relaxation (T_2) time weighted (echo time [TE] = 10 ms, repetition time [TR] = 3000 ms, 16 echos, in-plane resolution = 150 mm, 15 slices, slice thickness = 1 mm) images, whose intensity was weighted by one of the inherent timing parameters, spin-spin (T_2) relaxation, were acquired. The region for MR spectroscopy was positioned on a localized voxel ($0.6 \times 2 \times 2\,mm^3$) in the frontal cortex, positioned approximately 1 mm lateral and 1.5 mm posterior to the Bregma, encompassing major parts of the frontal cortex and minimizing overlap of the hippocampus and CSF (0.6 mm thickness). After uniformity of the magnetic field experienced within that chosen voxel was maximized using localized optimization techniques (> 5 min), water suppressed spectra of the chosen voxel were acquired using Point Resolved Spectroscopy (PRESS) sequence (NA = 512, total scan time = 25 min, TR/TE = 1500/16 ms, 4K data points, bandwidth = 150 Hz). The water suppressed MR data were processed and spectral chemical shifts were assigned with respect to the creatine peak (3.05 ppm). Analysis of the complex spectra was confined to those peaks that corresponded to creatine, glutamate (3.75 ppm), choline (3.22 ppm), *N*-acetyl aspartate (NAA, 2.06 ppm), *myo*-inositol (3.6 ppm) and GABA (2.28 ppm) – evaluated by deconvoluting those peaks to a Lorenzian line shape and calculating areas under those peaks proportional to metabolite concentrations within the chosen voxel. Spin-spin relaxation (T_2) maps were calculated using routines written in MATLAB (Mathworks). Areas from left and right hemispheres and each region (frontal, parietal) were averaged for each slice and subsequently averaged over all slices.

Mitochondrial fractionation

Cells harvested from 80 10-cm plates of nearly confluent cells were spun down at 1000 *g* at 4 °C for 10 min. Then, cells were resuspended in 20 ml ice-cold mitochondrial homogenization buffer (MHB; 20 mM HEPES, 1 mM EGTA, 75 mM sucrose, 225 mM mannitol, 2 mg/ml BSA) and left on ice for 5 min to swell. Cells were homogenized with a motorized Potter-Elvehjem homogenizer with 40-45 up/down strokes. To pellet nuclei and unbroken cells, homogenates were centrifuged (5 min, 600 *g*, 4 °C). Supernatants were centrifuged again for 5 min at 600 *g*, 4 °C to eliminate nuclei and debris. To pellet mitochondria, lysosomes and ER, supernatants were centrifuged for 10 min at 7000 *g*, 20,000 *g* and 100,000 *g*, respectively. Mitochondria pellets were washed 3 times with 20 ml of MHB buffer and centrifuged for 10 min at 10,000 *g*, 4 °C. Finally, the crude mitochondrial pellet was resuspended in 2.2 ml of mitochondrial resuspension buffer (MRB; 5 mM HEPES, 0.5 mM EGTA, 250 mM mannitol, 2 mg/ml BSA) and transferred into 8 ml of 30% Percoll (in 2× Percoll medium; 50 mM HEPES, 2 mM EGTA, 450 mM mannitol, 4 mg/ml BSA) and ultracentrifuged for 30 min at 95,000 *g*, 4 °C in a swinging bucket rotor (SW41Ti; Beckman). The mitochondrial band was collected in, and diluted with, 14 ml of MRB. Mitochondria were washed twice with 14 ml MRB and centrifuged for 10 min at 6300 *g*, 4 °C. Purified mitochondria were finally resuspended in 50–200 μl of MRB. Samples were quantified with Pierce BCA Protein Assay Reagent (Thermo Fisher Scientific) and analysed by SDS-PAGE.

Complex I enzyme activity assay

To measure complex I activity in MEFs, we used the Complex I Enzyme Activity Dipstick Assay Kit (MS130; Abcam) following the manufacturer's instructions. Briefly, cells were cultured and then lysed using a specific Extraction Buffer. Dipsticks were added and wicked for 30 min, then transferred to fresh activity buffer for 30 min to reveal the signal. Quantifications and imaging were carried out with Image Lab Software (BioRad).

Statistical analysis

Results are expressed as means ± SEM. Statistical analysis was performed using Student's *t*-test, assuming unequal variance, with $P < 0.05$ considered significant. Mann-Whitney *U*-statistics or one-way ANOVA test were used for comparisons among different data sets. Asterisks indicate significant differences ($^{*}P < 0.05$, $^{**}P < 0.01$, $^{***}P < 0.005$).

Supplementary Material

Supplementary Material is available at *HMG* online.

Acknowledgements

We thank V. Diaz and D. Donahue for assistance with the MRI and CT scans, respectively. We also thank M. Lussier, A. Koretsky and M. O'Donovan for scientific advice and stimulating discussions.

Conflict of Interest statement. None declared.

Funding

This work was supported by the Intramural Research Program of the National Institute of Neurological Disorders and Stroke, National Institutes of Health.

References

1. Blackstone, C., O'Kane, C.J. and Reid, E. (2011) Hereditary spastic paraplegias: membrane traffic and the motor pathway. *Nat. Rev. Neurosci.*, **12**, 31–42.
2. Blackstone, C. (2012) Cellular pathways of hereditary spastic paraplegia. *Annu. Rev. Neurosci.*, **35**, 25–47.
3. Tesson, C., Koht, J. and Stevanin, G. (2015) Delving into the complexity of hereditary spastic paraplegias: phenotypes and inheritance modes are revolutionizing their nosology. *Hum. Genet.*, **134**, 511–538.

4. Fink, J.K. (2013) Hereditary spastic paraplegia: clinico-pathologic features and emerging molecular mechanisms. *Acta Neuropathol.*, **126**, 307–328.
5. Harding, A.E. (1993) Hereditary spastic paraplegia. *Semin. Neurol.*, **13**, 333–336.
6. Novarino, G., Fenstermaker, A.G., Zaki, M.S., Hofree, M., Silhavy, J.L., Heiberg, A.D., Abdellateef, M., Rosti, B., Scott, E., Mansour, L., *et al.* (2014) Exome sequencing links corticospinal motor neuron disease to common neurodegenerative disorders. *Science*, **343**, 506–511.
7. Park, S.H., Zhu, P.P., Parker, R.L. and Blackstone, C. (2010) Hereditary spastic paraplegia proteins REEP1, spastin, and atlastin-1 coordinate microtubule interactions with the tubular ER network. *J. Clin. Invest.*, **120**, 1097–1110.
8. Gerondopoulos, A., Bastos, R.N., Yoshimura, S., Anderson, R., Carpanini, S., Aligianis, I., Handley, M.T. and Barr, F.A. (2014) Rab18 and a Rab18 GEF complex are required for normal ER structure. *J. Cell Biol.*, **205**, 707–720.
9. Hu, J., Shibata, Y., Zhu, P.P., Voss, C., Rismanchi, N., Prinz, W.A., Rapoport, T.A. and Blackstone, C. (2009) A class of dynamin-like GTPases involved in the generation of the tubular ER network. *Cell*, **138**, 549–561.
10. Voeltz, G.K., Prinz, W.A., Shibata, Y., Rist, J.M. and Rapoport, T.A. (2006) A class of membrane proteins shaping the tubular endoplasmic reticulum. *Cell*, **124**, 573–586.
11. Hu, J., Shibata, Y., Voss, C., Shemesh, T., Li, Z., Coughlin, M., Kozlov, M.M., Rapoport, T.A. and Prinz, W.A. (2008) Membrane proteins of the endoplasmic reticulum induce high-curvature tubules. *Science*, **319**, 1247–1250.
12. Tolley, N., Sparkes, I.A., Hunter, P.R., Craddock, C.P., Nuttall, J., Roberts, L.M., Hawes, C., Pedrazzini, E. and Frigerio, L. (2008) Overexpression of a plant reticulon remodels the lumen of the cortical endoplasmic reticulum but does not perturb protein transport. *Traffic*, **9**, 94–102.
13. Zhu, P.P., Patterson, A., Lavoie, B., Stadler, J., Shoeb, M., Patel, R. and Blackstone, C. (2003) Cellular localization, oligomerization, and membrane association of the hereditary spastic paraplegia 3A (SPG3A) protein atlastin. *J. Biol. Chem.*, **278**, 49063–49071.
14. Zhu, P.P., Soderblom, C., Tao-Cheng, J.H., Stadler, J. and Blackstone, C. (2006) SPG3A protein atlastin-1 is enriched in growth cones and promotes axon elongation during neuronal development. *Hum. Mol. Genet.*, **15**, 1343–1353.
15. Solowska, J.M., Morfini, G., Falnikar, A., Himes, B.T., Brady, S.T., Huang, D. and Baas, P.W. (2008) Quantitative and functional analyses of spastin in the nervous system: implications for hereditary spastic paraplegia. *J. Neurosci.*, **28**, 2147–2157.
16. Riano, E., Martignoni, M., Mancuso, G., Cartelli, D., Crippa, F., Toldo, I., Siciliano, G., Di Bella, D., Taroni, F., Bassi, M.T., *et al.* (2009) Pleiotropic effects of spastin on neurite growth depending on expression levels. *J. Neurochem.*, **108**, 1277–1288.
17. Beetz, C., Koch, N., Khundadze, M., Zimmer, G., Nietzsche, S., Hertel, N., Huebner, A.K., Mumtaz, R., Schweizer, M., Dirren, E., *et al.* (2013) A spastic paraplegia mouse model reveals REEP1-dependent ER shaping. *J. Clin. Invest.*, **123**, 4273–4282.
18. Züchner, S., Wang, G., Tran-Viet, K.N., Nance, M.A., Gaskell, P.C., Vance, J.M., Ashley-Koch, A.E. and Pericak-Vance, M.A. (2006) Mutations in the novel mitochondrial protein REEP1 cause hereditary spastic paraplegia type 31. *Am. J. Hum. Genet.*, **79**, 365–369.
19. Hewamadduma, C., McDermott, C., Kirby, J., Grierson, A., Panayi, M., Dalton, A., Rajabally, Y. and Shaw, P. (2009) New pedigrees and novel mutation expand the phenotype of *REEP1*-associated hereditary spastic paraplegia (HSP). *Neurogenetics*, **10**, 105–110.
20. Schottmann, G., Seelow, D., Seifert, F., Morales-Gonzalez, S., Gill, E., von Au, K., von Moers, A., Stenzel, W. and Schuelke, M. (2015) Recessive REEP1 mutation is associated with congenital axonal neuropathy and diaphragmatic palsy. *Neurol. Genet.*, **1**, e32.
21. Saito, H., Kubota, M., Roberts, R.W., Chi, Q. and Matsunami, H. (2004) RTP family members induce functional expression of mammalian odorant receptors. *Cell*, **119**, 679–691.
22. Behrens, M., Bartelt, J., Reichling, C., Winnig, M., Kuhn, C. and Meyerhof, W. Members of RTP and REEP gene families influence bitter taste receptor expression. *J. Biol. Chem.*, **281**, 20650–20659.
23. Björk, S., Hurt, C.M., Ho, V.K. and Angelotti, T. REEPs are membrane shaping adapter proteins that modulate specific G protein-coupled receptor trafficking by affecting ER cargo capacity. *PLoS One*, **8**, e76366.
24. Brady, J.P., Claridge, J.K., Smith, P.G. and Schnell, J.R. (2015) A conserved amphipathic helix is required for membrane tubule formation by Yop1p. *Proc. Natl. Acad. Sci. USA*, **112**, E639–E648.
25. Schlaitz, A.L., Thompson, J., Wong, C.C.L., Yates, J.R., 3rd. and Heald, R. (2013) REEP3/4 ensure endoplasmic reticulum clearance from metaphase chromatin and proper nuclear envelope architecture. *Dev. Cell*, **26**, 315–323.
26. Lim, Y., Cho, I.T., Schoel, L.J. and Golden, J.A. (2015) Hereditary spastic paraplegia-linked REEP1 modulates endoplasmic reticulum/mitochondria contacts. *Ann. Neurol.*, **78**, 679–696.
27. Goyal, U. and Blackstone, C. (2013) Untangling the web: mechanisms underlying ER network formation. *Biochim. Biophys. Acta*, **1833**, 2492–2498.
28. Westrate, L.M., Lee, J.E., Prinz, W.A. and Voeltz, G.K. (2015) Form follows function: the importance of endoplasmic reticulum shape. *Annu. Rev. Biochem.*, **84**, 791–811.
29. Walther, T.C. and Farese, R.V. Jr. (2012) Lipid droplets and cellular lipid metabolism. *Annu. Rev. Biochem.*, **81**, 687–714.
30. Klemm, R.W., Norton, J.P., Cole, R.A., Li, C.S., Park, S.H., Crane, M.M., Li, L., Jin, D., Boye-Doe, A., Liu, T.Y., *et al.* (2013) A conserved role for atlastin GTPases in regulating lipid droplet size. *Cell Rep.*, **3**, 1465–1475.
31. Falk, J., Rohde, M., Bekhite, M.M., Neugebauer, S., Hemmerich, P., Kiehntopf, M., Deufel, T., Hübner, C.A. and Beetz, C. (2014) Functional mutation analysis provides evidence for a role of REEP1 in lipid droplet biology. *Hum. Mutat.*, **35**, 497–504.
32. Papadopoulos, C., Orso, G., Mancuso, G., Herholz, M., Gumeni, S., Tadepalle, N., Jüngst, C., Tzschichholz, A., Schauss, A., Höning, S., *et al.* (2015) Spastin binds to lipid droplets and affects lipid metabolism. *PLoS Genet.*, **11**, e1005149.
33. Szymanski, K.M., Binns, D., Bartz, R., Grishin, N.V., Li, W.P., Agarwal, A.K., Garg, A., Anderson, R.G.W. and Goodman, J.M. (2007) The lipodystrophy protein seipin is found at endoplasmic reticulum lipid droplet junctions and is important for droplet morphology. *Proc. Natl. Acad. Sci. USA*, **104**, 20890–20895.
34. Rinaldi, C., Schmidt, T., Situ, A.J., Johnson, J.O., Lee, P.R., Chen, K., Bott, L.C., Fadó, R., Harmison, G.H., Parodi, S., *et al.* (2015) Mutation in *CPT1C* associated with pure autosomal dominant spastic paraplegia. *JAMA Neurol.*, **72**, 561–570.
35. Fulton, B.P. and Walton, K. (1986) Electrophysiological properties of neonatal rat motoneurones studied in vitro. *J. Physiol.*, **370**, 651–678.

36. Gonzalez, M., Nampoothiri, S., Kornblum, C., Oteyza, A.C., Walter, J., Konidari, I., Hulme, W., Speziani, F., Schöls, L., Züchner, S. and Schüle, R. (2013) Mutations in phospholipase DDHD2 cause autosomal recessive hereditary spastic paraplegia (SPG54). *Eur. J. Hum. Genet.*, **21**, 1214–1218.
37. Ulengin, I., Park, J.J. and Lee, T.H. (2015) ER network formation and membrane fusion by atlastin1/SPG3A disease variants. *Mol. Biol. Cell*, **26**, 1616–1628.
38. Marcinkiewicz, A., Gauthier, D., Garcia, A. and Brasaemle, D.L. (2006) The phosphorylation of serine 492 of perilipin a directs lipid droplet fragmentation and dispersion. *J. Biol. Chem.*, **281**, 11901–11909.
39. Hefferan, M.P., Kucharova, K., Kinjo, K., Kakinohana, O., Sekerkova, G., Nakamura, S., Fuchigami, T., Tomori, Z., Yaksh, T.L., Kurtz, N. and Marsala, M. (2007) Spinal astrocyte glutamate receptor 1 overexpression after ischemic insult facilitates behavioral signs of spasticity and rigidity. *J. Neurosci.*, **27**, 11179–11191.
40. Tian, G.F., Azmi, H., Takano, T., Xu, Q., Peng, W., Lin, J., Oberheim, N., Lou, N., Wang, X., Zielke, H.R., *et al.* (2005) An astrocytic basis of epilepsy. *Nat. Med.*, **11**, 973–981.
41. Holm, C. (2003) Molecular mechanisms regulating hormone-sensitive lipase and lipolysis. *Biochem. Soc. Trans.*, **31**, 1120–1124.
42. Yeaman, S.J. (2004) Hormone-sensitive lipase–new roles for an old enzyme. *Biochem. J.*, **379**, 11–22.
43. Toh, S.Y., Gong, J., Du, G., Li, J.Z., Yang, S., Ye, J., Yao, H., Zhang, Y., Xue, B., Li, Q., *et al.* (2008) Up-regulation of mitochondrial activity and acquirement of brown adipose tissue-like property in the white adipose tissue of *Fsp27* deficient mice. *PLoS One*, **3**, e2890.
44. Peng, X.G., Ju, S., Fang, F., Wang, Y., Fang, K., Cui, X., Liu, G., Li, P., Mao, H. and Teng, G.J. (2013) Comparison of brown and white adipose tissue fat fractions in *ob*, *seipin*, and *Fsp27* gene knockout mice by chemical shift-selective imaging and ^{1}H-MR spectroscopy. *Am. J. Physiol. Endocrinol. Metab.*, **304**, 160–167.
45. Gross, D.A., Snapp, E.L. and Silver, D.L. (2010) Structural insights into triglyceride storage mediated by fat storage-inducing transmembrane (FIT) protein 2. *PLoS One*, **5**, e10796.
46. DeBose-Boyd, R.A. (2008) Feedback regulation of cholesterol synthesis: sterol-accelerated ubiquitination and degradation of HMG CoA reductase. *Cell Res.*, **18**, 609–621.
47. Agarwal, A.K. and Garg, A. (2006) Genetic disorders of adipose tissue development, differentiation, and death. *Annu. Rev. Genomics Hum. Genet.*, **7**, 175–199.
48. Boutet, E., El Mourabit, H., Prot, M., Nemani, M., Khallouf, E., Colard, O., Maurice, M., Durand-Schneider, A.M., Chrétien, Y., Grès, S., *et al.* (2009) Seipin deficiency alters fatty acid Δ9 desaturation and lipid droplet formation in Berardinelli-Seip congenital lipodystrophy. *Biochimie*, **91**, 796–803.
49. Chen, W., Yechoor, V.K., Chang, B.H.J., Li, M.V., March, K.L., and Chan, L. The human lipodystrophy gene product Berardinelli-Seip congenital lipodystrophy 2/seipin plays a key role in adipocyte differentiation. *Endocrinology*, **150**, 4552–4561.
50. Fei, W., Du, X. and Yang, H. (2011) Seipin, adipogenesis and lipid droplets. *Trends Endocrinol. Metab.*, **22**, 204–210.
51. Payne, A.V., Grimsey, N., Tuthill, A., Virtue, S., Gray, S.L., Dalla Nora, E., Semple, R.K., O'Rahilly, S. and Rochford, J.J. (2008) The human lipodystrophy gene *BSCL2/Seipin* may be essential for normal adipocyte differentiation. *Diabetes*, **57**, 2055–2060.
52. Cui, X., Wang, Y., Meng, L., Fei, W., Deng, J., Xu, G., Peng, X., Ju, S., Zhang, L., Liu, G., *et al.* (2012) Overexpression of a short human seipin/BSCL2 isoform in mouse adipose tissue results in mild lipodystrophy. *Am. J. Physiol. Endocrinol. Metab.*, **302**, 705–713.
53. Chen, W., Chang, B., Saha, P., Hartig, S.M., Li, L., Reddy, V.T., Yang, Y., Yechoor, V., Mancini, M.A.,. and Chan, L. (2012) Berardinelli-Seip congenital lipodystrophy 2/seipin is a cell-autonomous regulator of lipolysis essential for adipocyte differentiation. *Mol. Cell. Biol.*, **32**, 1099–1111.
54. Prieur, X., Dollet, L., Takahashi, M., Nemani, M., Pillot, B., Le May, C., Mounier, C., Takigawa-Imamura, H., Zelenika, D., Matsuda, F., *et al.* (2013) Thiazolidinediones partially reverse the metabolic disturbances observed in *Bscl2*/seipin-deficient mice. *Diabetologia*, **56**, 1813–1825.
55. Fei, W., Shui, G., Gaeta, B., Du, X., Kuerschner, L., Li, P., Brown, A.J., Wenk, M.R., Parton, R.G. and Yang, H. (2008) Fld1p, a functional homologue of human seipin, regulates the size of lipid droplets in yeast. *J. Cell Biol.*, **180**, 473–482.
56. Rismanchi, N., Soderblom, S., Stadler, J., Zhu, P.P. and Blackstone, C. (2008) Atlastin GTPases are required for Golgi apparatus and ER morphogenesis. *Hum. Mol. Genet.*, **17**, 1591–1604.
57. Thiam, A.R., Farese, R.V., Jr. and Walther, T.C. (2013) The biophysics and cell biology of lipid droplets. *Nat. Rev. Mol. Cell Biol.*, **14**, 775–786.
58. Appocher, C., Klima, R. and Feiguin, F. (2014) Functional screening in Drosophila reveals the conserved role of REEP1 in promoting stress resistance and preventing the formation of tau aggregates. *Hum. Mol. Genet.*, **23**, 6762–6772.
59. Renvoisé, B., Stadler, J., Singh, R., Bakowska, J.C. and Blackstone, C. (2012) *Spg20-/-* mice reveal multimodal functions for Troyer syndrome protein spartin in lipid droplet maintenance, cytokinesis and BMP signaling. *Hum. Mol. Genet.*, **21**, 3604–3618.
60. Spandl, J., White, D.J., Peychl, J. and Thiele, C. (2009) Live cell multicolor imaging of lipid droplets with a new dye, LD540. *Traffic*, **10**, 1579–1584.
61. Blivis, D. and O'Donovan, M.J. (2012) Retrograde loading of nerves, tracts, and spinal roots with fluorescent dyes. *J. Vis. Exp.*, pii: 4008.